Journal of Manufacturing Processes 168 (2026) 439–450

Contents lists available at ScienceDirect

Journal of Manufacturing Processes

journal homepage: www.elsevier.com/locate/manpro

Exploiting the SPH meshless approach potential for Tube Friction Stir Extrusion: insights into process mechanics, grain size, and micro-mechanical properties

Salvatore Russo [a], Riccardo Puleo [a], Gianluca Buffa [a,*], Livan Fratini [a]

[a] *Department of Engineering, University of Palermo, Viale delle Scienze, Palermo, 90128, Italy*

HIGHLIGHTS

- A SPH meshless model was developed to simulate tube Friction Stir Extrusion.
- The model was validated through experimental temperature and force measurements.
- SPH reveals transient material mixing mechanisms during FSE tube forming.
- Distinct grain and hardness gradients were predicted across tube thickness.
- Framework enables microstructure prediction and improved FSE process design.

GRAPHICAL ABSTRACT

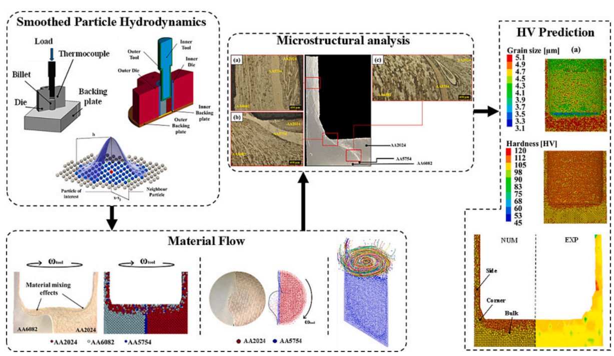

ARTICLE INFO

Keywords:
FSE
Aluminum
SPH
Tube
Solid state

ABSTRACT

Friction stir-based manufacturing processes have recently attracted increasing attention due to their ability to process aluminum without melting, potentially reducing energy consumption compared to conventional routes. Among these, Friction Stir Extrusion (FSE) has emerged as an effective technique for producing metal wires, and more recently, its potential has also been explored for tube manufacturing applications. This paper aims to provide an insight into tube production through the FSE process by developing a dedicated numerical model using the Smoothed Particle Hydrodynamics (SPH) technique. The model was first validated against experimental temperature and load measurements and then used to (i) investigate the complex material flow occurring during the process, through the analysis of dissimilar three-material tubes; (ii) investigate the effect of tool rotation on the main microstructural and micro-mechanical properties of the tubes, i.e., grain size and microhardness. The results indicate that two regions can be identified across the tube thickness, namely an inner one, characterized by higher deformation, smaller grain size, and higher microhardness, and the outer one, where elongated grains and lower microhardness values are observed. Overall, the FSE process proved to be a valid, sustainable alternative for tube manufacturing, while SPH modelling offers high accuracy and effectiveness on microstructure and hardness prediction.

* Corresponding author.
E-mail address: Gianluca.buffa@unipa.it (G. Buffa).

https://doi.org/10.1016/j.jmapro.2026.04.002
Received 30 March 2026; Accepted 2 April 2026
Available online 17 April 2026
1526-6125/© 2026 The Authors. Published by Elsevier Ltd on behalf of The Society of Manufacturing Engineers. This is an open access article under the CC BY license (http://creativecommons.org/licenses/by/4.0/).

1. Introduction

Over the last decade, the aim to reduce product weight while maintaining high strength has led automotive and aerospace industries to increasingly replace steel with aluminum and its alloys, mainly because of the higher strength-to-weight ratio that characterizes these materials. Although the mechanical performance and the weight saving of aluminum are convenient, its primary production has a significant environmental impact [1,2]. In response to recent sustainability goals, increasing attention has been devoted to solid-state manufacturing processes, which can significantly reduce energy consumption by avoiding melting. Among these, friction stir–based techniques have attracted considerable interest due to their relative simplicity, process robustness, and potential for energy-efficient material processing. Friction Stir Extrusion (FSE) belongs to this class of solid-state, friction-driven processes, enabling severe plastic deformation and material consolidation through intense shear under controlled thermal conditions. Friction Stir Extrusion (FSE) has traditionally been used to produce consolidated wires. Baffari et al. [3] investigated the influence of the main process parameters and the initial temper of the base material on the process on the extrudates' mechanical properties. Behnagh et al. [4] observed dynamic recrystallized grain structure in friction-extruded wires produced from Mg chips. Whalen et al. [5] obtained aluminum rods from Al-12.4TM powder. They were able to produce 5 mm diameter rods with a higher elongation than rods of the same material obtained by conventional extrusion. Li et al. [6] highlighted the process mechanics of FSE by experimentally measuring strain and strain rate through the use of a proper marker.

Recently, FSE has also been explored for tube manufacturing. Behnagh et al. [7] produced tubes using a double-step approach, where chips were consolidated and then extruded. In addition, Swarnkar et al. [8] investigated the bi-material tube production using different materials.

Production of tubes via FSE is still an active research topic, as the complex process mechanics, as well as the mutual interactions between the main process variables (i.e., tool force, tool rotation, and tool geometry), are still mainly unclear. In this way, fundamental knowledge of the process is needed, and numerical simulation can represent a useful tool for proper process comprehension and design. Only a very few papers can be found in the literature focused on the numerical simulation of the FSE of tubes. Asadi et al. [9] developed a FEM model of the process to study the influence of the tool geometry on the main field variables' distribution in the FSE of Al—Si tubes.

Although the FEM technique has conventionally been adopted for studying several manufacturing processes, it demonstrates severe limitations in modelling (i) processes in which the material undergoes extremely high levels of strain, requiring extremely fine mesh and several remesh steps, and resulting in non-affordable computational times, and/or (ii) processes involving multi-material workpieces. These limitations can be overcome by mesh-free approaches, developed in the last few years. Among the emerging techniques, the Smoothed Particle Hydrodynamics (SPH) method has attracted particular interest due to its distinctive characteristics. Smoothed Particle Hydrodynamics, first employed by Lucy [10], and Gingold and Monaghan [11] for astrophysical analyses, is a numerical method based on a truly Lagrangian approach [12]. In this method, field variables are determined through functions that are discretized and averaged using specific kernel functions [13]. Currently, literature has demonstrated the application of the SPH method as a robust solution for addressing diverse computational challenges. Due to its exceptional capability in handling large deformations, SPH has been extensively employed in impact analysis studies [14]. More recently, following the enhancement and extension of these models to thermomechanical analyses [15,16], the SPH method has been successfully applied to a few manufacturing processes. Zhilang et al. [17] modeled solid bonding phenomena by simulating the Cold Spray process, which involves partial melting, interface instabilities, and oxide fracture. Hisaya Komen et al. [18] applied the incompressible SPH formulation to gas metal arc welding, focusing on molten metal flow tracking and heat conduction. Ali Nassiri et al. [19], Z.L. Zhang et al. [20], and Ming Yang et al. [21] modeled solid bonding phenomena in impact welding using smoothed particle hydrodynamics, accurately capturing the fundamental mechanisms occurring in these processes. Lei Li et al. [22] developed a model that allowed enhanced understanding of the material flow at the die interface during friction stir welding, a process in which material mixing at the interface of different components under high pressures and temperatures induces solid-state bonding. Some of the same authors [23] applied the SPH method to wire production, achieving a deeper understanding of the relationship between process parameters and process output. In addition, through appropriate material tracers, they successfully validated numerical flow

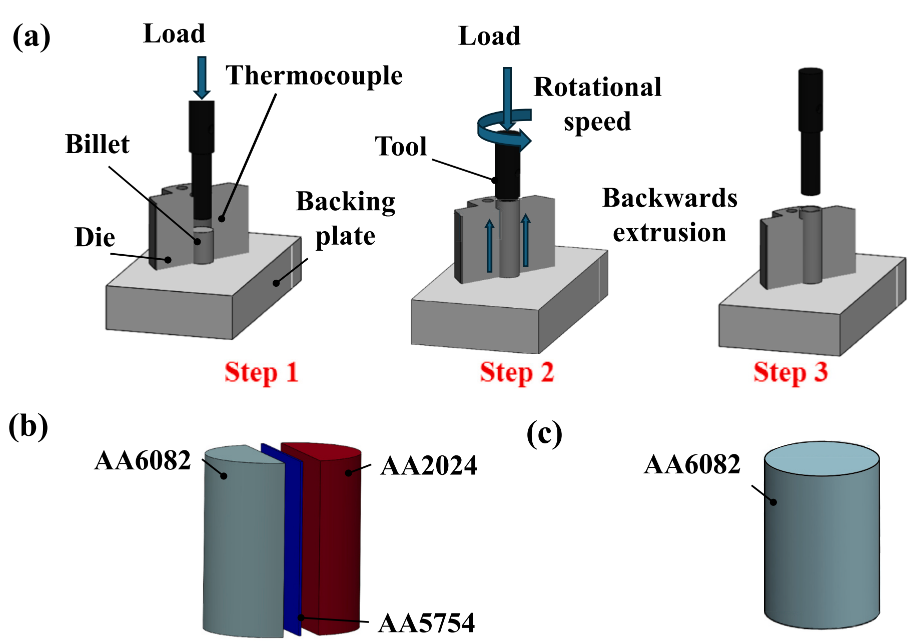

Fig. 1. (a) Experimental setup and process steps, (b) samples used for the material flow investigation, (c) solid aluminum sample.

Table 1
Process parameter combinations for the microstructure and material flow investigations.

ID	Rotational speed [rpm]	Vertical load [kN]	Target
ID1	1000	12	Microstructure
ID2	1500	12	
ID3	2000	12	
ID4	1500	5	Material flow

predictions against experimental results.

To the author's knowledge, only one study [23] has investigated the phenomena occurring during solid-state tube formation using the SPH method. In that work, the authors employed the ShAPE process to produce tubes. In this process, a rotating die is plunged into confined feedstock material, such as powders, metal chips, or bulk billets, plasticizing it through rotational shear. The application of the SPH method to the ShAPE tube-forming process enabled the determination of the steady-state distribution of the main process variables. However, further study is necessary to comprehensively understand the complex material flow occurring, with particular attention to the transient starting phase and the actual material mixing. As a matter of fact, the latter topics which have not yet been subject to specific numerical investigation so far, are crucial for the full comprehension of the process and the prediction of the tubes overall mechanical properties, which are a direct consequence of the material properties after the process, i.e. grain size and microhardness, that, in their turn, can be predicted based on the main field variables distribution.

In this paper, a dedicated numerical SPH model was developed to reproduce and investigate tube manufacturing via FSE. The final aim was to propose an accurate tool capable of providing (i) fundamental knowledge on the process mechanics by investigating the occurring material flow, and (ii) predicting the tubes' main microstructural and micro-mechanical properties, such as grain and hardness evolution, starting from the process input parameters. AA2024 tubes were produced from a commercial bulk workpiece as reference samples, while the material flow was investigated by analyzing a three-material tube. For the production of the latter, the starting billet was assembled by considering two half-cylinders, made of AA2024 and AA6082, respectively, with a thin AA5754 sheet between the two halves to track the materials distribution during the process.

2. Methodology

2.1. Experimental campaign

The experimental campaigns were carried out using an ESAB LEGIO machine, originally designed for friction stir welding processes and adapted for FSE. The experimental setup included a backing plate supporting a custom-designed die with an inner chamber measuring 76 mm in height and 25 mm in diameter, together with an extruding tool 22 mm in diameter. In addition, in order to monitor the process and validate the numerical model, a K-thermocouple was placed at 1/3 of the die height, at a distance of 1 mm from the inner surface.

All the tests (i.e., single material and three-material tubes) were carried out with force control on the tool, following the same FSE steps (Fig. 1a). First, the tool was brought into contact with the specimen under a pre-load equal to 5 kN. Then, the FSE was initiated using the parameter combinations indicated in Table 1, and finally, the tool was lifted, and the tube extracted. The actual FSE process (Step 2, Fig. 1a) was also divided into two stages. In the first stage, a vertical load equal to 5 kN and a designed rotational speed were applied to generate sufficient heat input for material softening. After a dwell time equal to 5 s, the axial force progressively increased to the target value at the rate of 0.5 kN/s and was maintained until the end of the process. This experimental procedure was derived from previous experimental campaigns.

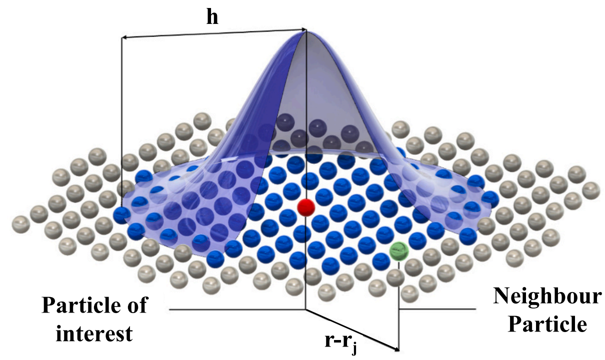

Fig. 2. Sketch of the smoothing kernel function, showing the weighting of neighboring particles within the support domain defined by the smoothing length *h*.

The samples used for the material flow investigation consisted of three components (Fig. 1b): half-cylinder made of AA2024, half-cylinder made of AA6082, and a sheet marker of AA5754. In order to investigate the onset of the material flow, three stop tests were carried out, stopping the process after 5, 7, and 10 s (ID4). Additionally, a fully extruded tube was cut along the longitudinal section for studying the material distribution (ID4 fully extruded). On the other hand, a solid AA2024 cylinder 25 mm in diameter and 35 mm in height was used for the microstructural investigation (Fig. 1c), and the longitudinal section of the produced tube was studied (ID1 to ID3). It is worth noting that solid material was selected instead of scrap in order to speed up the simulation campaign. As demonstrated, solid bonding occurs below the tool in the early stage of the process [24,25] in this way, process mechanics and main field variables distribution are not significantly affected by the different nature of the billet material.

After the specimens were extracted, they were mounted, polished, and etched using Keller's reagent, composed of 2 ml HF, 3 ml HCl, 5 ml HNO_3, and 190 ml H_2O. The grain size was determined using an Olympus GX51 optical microscope and analyzed in accordance with ASTM E112–13. Grain boundaries were automatically detected, and grain diameters were computed using automated image analysis, ensuring reproducible and standardized measurements [26].

Micro-hardness characterization was carried out using a Struers Duramin-40 machine, though an automatic indentation along the entire surface of the sample.

2.2. SPH Formulation and numerical model

2.2.1. Governing equations

The computational framework employed in this study is based on the Smoothed Particle Hydrodynamics (SPH) method, a mesh-free Lagrangian technique. The fundamental governing equations (Eq. 1–3) to be solved are derived from the conservation principles of continuum mechanics, i.e., the conservation of mass, momentum, and energy [10]:

$$\frac{D\rho}{Dt}+\rho\nabla\cdot\mathbf{v}=0 \tag{1}$$

$$\rho\frac{D\mathrm{v}}{Dt}=\nabla\cdot\boldsymbol{\sigma}+\rho\mathbf{b} \tag{2}$$

$$\rho C_p\frac{DT}{Dt}=\nabla\cdot(k\nabla T)+\dot{\mathbf{q}} \tag{3}$$

where ρ denotes the material density, t is time, **v** is the velocity field, **σ** is the Cauchy stress tensor, **b** is the body forces per unit mass, D is the rate of deformation tensor, C_p is the heat capacity, k is the thermal conductivity, T is the temperature, and $\dot{\mathbf{q}}$ denotes the heat flux vector.

In the SPH simulation, field variables are approximated through kernel interpolation, where each particle's contribution is weighted by a smoothing kernel function that depends on the distance between neighboring (Fig. 2).

For any function f(x), the SPH approximation is expressed as:

$$\langle f(\mathrm{x}) \rangle = \sum_{j=1}^{N} \frac{m_j}{\rho_j} f(\mathrm{x}_j) W(|\mathrm{x}-\mathrm{x}_j|, h) \tag{4}$$

where $W(|\mathrm{x}-\mathrm{x}_j|, h)$ is the smoothing kernel function, which depends on the distance between the position of the particle of interest x and that of a neighboring particle x_j, h is the smoothing length, m_j and ρ_j are the mass and density of the j, and N is the total number of neighboring particles within the support domain.

The gradient of any field variable is computed as:

$$\langle \nabla f(\mathrm{x}) \rangle = \sum_{j=1}^{N} \frac{m_j}{\rho_j} f(\mathrm{x}_j) \nabla W(|\mathrm{x}-\mathrm{x}_j|, h) \tag{5}$$

It is worth noting that this mesh-free formulation, by abolishing the need for explicit connectivity between particles, offers substantial advantages in modelling extreme deformations and material separation phenomena.

The SPH interpolation is performed using the cubic B-spline kernel function, expressed as:

$$W(\mathbf{x}, h) = C \begin{cases} 1 - \frac{3}{2}x^2 + \frac{3}{4}\mathrm{x} & |x| \leq 1 \\ \frac{1}{4}(2-x) & 1 \leq |\mathrm{x}| \leq 2 \\ 0 & 2 < |x| \end{cases} \tag{6}$$

where C is a normalization constant that depends on the number of spatial dimensions. For this three-dimensional analysis, the considered value was $C=\pi h^3$.

This selection followed a sensitivity analysis comparing quadratic, quartic, and quintic kernels, identifying the cubic B-spline as the optimal balance between numerical stability and computational cost.

Two smoothing length management strategies were implemented. Initially, $h = 1.3\,\Delta x$ was kept constant, with Δx representing the initial particle spacing. For enhanced accuracy in regions experiencing significant density variations, a variable smoothing length formulation was adopted, in which h evolves according to [11]:

$$h_i = h_0 \left(\frac{\rho_0}{\rho_i}\right)^{1/d} \tag{7}$$

where $h_0$and $\rho_0$are the initial smoothing length and density, respectively, and $d$is the spatial dimension.

It is observed that, owing to the Lagrangian nature of SPH, particles move with material velocity, naturally preserving material objectivity and removing convective terms from the governing equations. This intrinsic feature also facilitates accurate tracking of material history variables, which is essential for path-dependent constitutive models.

2.2.2. Constitutive modelling

The material behavior is described through an elastoplastic constitutive model with isotropic hardening. The total deformation is additively decomposed into elastic and plastic components:

$$D = \mathrm{D}^e + \mathrm{D}^p \tag{8}$$

Elastic deformations are governed by Hooke's law, while plastic deformations are activated upon satisfaction of the yield criterion. The plastic flow behavior is characterized by the Johnson-Cook constitutive model (Eq. 9) with isotropic hardening, accounting for strain hardening, strain rate sensitivity, and thermal softening effects:

$$\sigma_y = [A + B(\bar{\varepsilon}^p)^n]\left[1 + Cln\left(\frac{\dot{\varepsilon}^p}{\dot{\varepsilon}_0}\right)\right]\left[1 - \left(\frac{T - T_{room}}{T_{melt} - T_{room}}\right)^m\right] \tag{9}$$

where σ_y is the flow stress, $\bar{\varepsilon}^p$is the equivalent plastic strain, $\dot{\varepsilon}^p$ is the plastic strain rate, A, B, C, n, and m are material-dependent constants, and $\dot{\varepsilon}_0$is the reference strain rate. T denotes the current temperature, while T_{room} and T_{melt} represent the room and melting temperatures, respectively.

The non-saturating strain-hardening behavior of the Johnson-Cook model often leads to an overestimation of flow stress at high strain levels. To mitigate this issue, the procedure outlined in [22,27] was implemented, considering the experimentally determined initial yield stress as parameter A, with the strain-hardening parameters B and n suppressed.

2.2.3. Contact Mechanics and Friction Modelling

The interaction between the forming tool and the workpiece is governed by contact mechanics algorithms implemented within the SPH framework. A soft constraint penalty formulation was employed for contact detection and enforcement. When penetration of workpiece particles into the tool surface is detected, a penalty force proportional to the penetration depth is applied:

$$\mathrm{F}_{penalty} = -k_{cs}\delta\mathrm{n} \tag{10}$$

In which δ represents the penetration depth, n is the outward unit normal vector to the tool surface, and k_{cs} denotes the contact stability stiffness, defined as the maximum value between the standard penalty (calculated starting from the material Young's modulus) and soft constraint formulations, which is evaluated as:

$$k_{cs}(t) = S_f \cdot m^* \cdot \left(\frac{1}{\Delta t_c(t)}\right)^2 \tag{11}$$

Where S_f is the scale factor for the soft constraint penalty formulation, m* represents a weighted function of the mass of the tracked particle and its neighboring reference nodes, and Δt_c is the contact time step, initially set equal to the solution time step. To maintain numerical stability, Δt_c is adaptively reset to the current time step whenever the solution time step increases, ensuring the penalty stiffness remains properly scaled and preventing unstable contact behavior.

The frictional resistance at the tool-workpiece interface was modeled using a combined Coulomb-Tresca friction law, which transitions between sliding and sticking conditions [28] based on local contact pressures:

$$\tau_f = \min\left(\mu\sigma_n, \frac{\sigma_y}{\sqrt{3}}\right) \tag{12}$$

where τ_f is the frictional shear stress, μ is the Coulomb friction coefficient, σ_n is the normal contact pressure, and $\sigma_y/\sqrt{3}$ represents the maximum shear stress according to the Von Mises criterion. This formulation ensures physically realistic friction behavior across sliding and sticking regimes. A sensitivity analysis conducted in the range 0.26–0.54 identified 0.39 as the optimal friction coefficient: values below 0.26 resulted in insufficient stirring (resembling simple extrusion), while values above 0.54 led to excessive plastic deformation.

2.2.4. Heat generation and thermal coupling

The primary heat generation mechanism arises from plastic deformation of the workpiece material. The rate of heat generation due to plastic work is governed by:

$$\dot{q}_{plastic} = \beta\sigma : \mathrm{D}^p \tag{13}$$

where β is the Taylor-Quinney coefficient, representing the fraction of plastic work converted to heat. Based on experimental observations for metallic materials, $\beta = 0.9$ is adopted [29], indicating that 90% of plastic deformation energy is dissipated as heat, with the remainder stored as latent energy in microstructural defects.

At the tool-workpiece interface, frictional sliding generates significant heat according to:

$$\dot{q}_{friction} = \eta_{friction} \tau_f |v_{rel}| \tag{14}$$

where $\eta_{friction}$ is the heat conversion coefficient (set to 0.9), and v_{rel} is the relative sliding velocity. The generated frictional heat is partitioned between the tool and workpiece according to their thermophysical properties. The fraction of heat absorbed by each body is determined by the following relation:

$$f = \frac{1}{1 + \frac{\sqrt{\rho C_p k_{Sb}}}{\sqrt{\rho C_p k_{Sa}}}} \tag{15}$$

where ρ, C_p and k is related to contact "a" and "b" surfaces. In the present analysis, a value of $f = 0.7$ was assigned according to the materials' thermo-physical characteristics.

The thermal interaction between the billet and the die was modeled through heat conduction across the contact interface. The heat transfer is governed by the temperature gradient and the contact conductance, which depends on pressure, surface conditions, and relative motion. This formulation allows an accurate representation of the thermal exchange during the process. For the present analysis, considering the pressure variation and the temperatures involved, a constant interfacial heat transfer coefficient of 147 W/m^2K [30] was assumed between the two components.

2.2.5. *Numerical prediction of grain size and microhardness*

To predict the grain size, a widely accepted relationship was used, based on the Zener-Hollomon parameter [31]:

$$\delta^{-m} = A + B \ln Z \tag{16}$$

where Z, the Zener-Hollomon parameter, is defined as:

$$Z = \dot{\varepsilon} \exp\left(\frac{Q}{RT}\right) \tag{17}$$

Where R is the universal gas constant and Q is the grain boundary activation energy [32], equal to 135,000 [J/mol]. In this model, the relationship between grain size and the deformation parameters is expressed as a function of the Zener-Hollomon parameter, with A, B, and m [32], representing empirical constants equal to −0.1696, 0.0153, and − 1.25, respectively [31]. Starting from the average grain diameter δ, the mechanical properties of the material can be effectively predicted. Specifically, the relationship between yield strength σy and grain size can be quantitatively described by the Hall-Petch relationship:

$$\sigma_y = \sigma_0 + k_y \cdot d^{-1/2} \tag{18}$$

which is valid for polycrystalline materials, where σy denotes the yield strength, d the average grain diameter, $\sigma_0$the intrinsic yield strength, representing the baseline resistance to dislocation motion, and ky material constant quantifying the effectiveness of grain boundaries as barriers to dislocation movement. In turn, yield strength and Vickers hardness are strongly correlated through the Tabor relation [33], expressed as $\sigma \approx C \cdot H_v$. The constraint factor C, typically approximated as $C \approx 3$ for most metals, it enables the Hall-Petch equation to be reformulated directly in terms of hardness:

$$H_v = H_0 + k_H \cdot d^{-1/2} \tag{19}$$

where $H_0$is the intrinsic hardness (approximately $\sigma_0/3$) and k_H is the specific Hall-Petch slope parameter for hardness.

For the AA2024-T351 alloy examined in this investigation, the Hall-Petch parameters were derived from a critical review of the literature. In accordance with previous studies on alloys of similar composition [34], the parameters were carefully selected to capture the complex interplay of hardening and softening mechanisms (e.g., dislocation density accumulation and dynamic recovery) characteristic of the friction stir processing conditions simulated. Specifically, an intrinsic yield strength of $\sigma_0 = 262$ MPa was adopted [34], which, according to Tabor's relation, corresponds to an intrinsic hardness of $H_0 \approx 87$ HV. Similarly, the Hall-Petch slope parameter, reflecting the high dislocation density expected from this process, was identified as $k_H = 39$ HV$\cdot$ $\mu m^{1/2}$ [35].

The calibrated Hall-Petch model (Eq. 19) was subsequently employed as a post-processing tool. The predicted average grain diameter from each numerical simulation was utilized as the input to calculate the final predicted hardness.

To validate the robustness of the integrated framework, a two-step rigorous procedure was followed, wherein the predicted average grain diameters were first compared against experimental microstructural

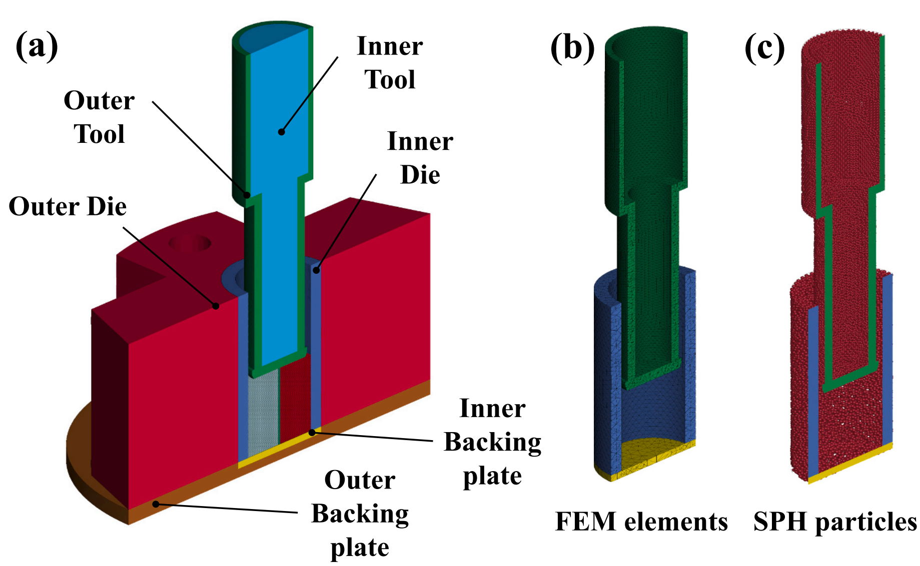

Fig. 3. (a) Numerical process modelling and tool-die discretization:
(b) rigid tetrahedral elements, and (c) SPH particles embedded in rigid domains for thermal coupling.

Table 2
Material physical and mechanical properties [40,41].

		Unit	AA2024-T351	AA6082-T6	AA5754	AISI-H13
Young's modulus	*E*	GPa	72.4	68.0	71.7	200
Poisson's ratio	*ν*	(−)	0.33	0.33	0.33	0.3
Density	*ρ*	Kg/m3	2785	2705	2650	7800
Conductivity	*k*	W/m K	188	7.62 + 0.995 T-17 × 10^{-4} T^2 + 1 × 10^{-6} T^3	120	24.5
Specific heat	*Cp*	J/g K	0.76688 + 3 × 10^{-4} T-2 × 10^{-7} T^2	0.7067 + 6 × 10^{-4} T-1 × 10^{-7} T^2	0.900	0.466

Table 3
Parameters of the Johnson-Cook constitutive equation of the aluminum alloys under analysis [37–39].

Parameter	Unit	AA2024-T351	AA6082-T6	AA5754
A	MPa	265	428.5	217
B	MPa	0	0	0
n	(−)	0	0	0
C	(−)	0.015	0.00747	0.135
m	(−)	1	1.31	1.561
T_m	K	823.15	823.15	823.15
T_r	K	293.15	293.15	293.15

data to confirm the accuracy of the underlying simulation, and subsequently, the predicted hardness values, derived via the calibrated Hall-Petch relation, were correlated with the experimental validation dataset.

2.2.6. Numerical model

The numerical simulations were carried out on a workstation equipped with a 12-core Intel Core i9 (12th generation) processor operating in symmetric multiprocessing (SMP) mode and 64 GB of RAM. The longest complete simulation of the extrusion process required a total CPU time of 49 h.

The numerical analyses were performed using the commercial finite element software LS-DYNA, where the mechanical equations were integrated in time with an explicit integration scheme, which is well suited to the highly nonlinear and transient dynamics characteristic of material deformation processes. The explicit integration imposes a stability constraint on the maximum permissible time step, governed by the Courant-Friedrichs-Lewy (CFL) condition:

$$\Delta t_{mech} \le C_{CFL} min\left(\frac{h}{c_s + |v|_{max}}\right) \tag{20}$$

where c_s is the local sound speed, C_{CFL} is the Courant number and $|v|_{max} = \max_i|\mathbf{v}_i|$denotes the maximum nodal velocity within the computational domain. To maintain a stable and efficient computation, a conservative fixed time step of $\Delta t_{mech} = 5\times 10^{-4}$s was adopted throughout the mechanical analysis. This fixed value was ensured by applying mass scaling based on a Courant number of $C_{CFL} = 0.5$, which allowed maintaining numerical stability without compromising the accuracy of the dynamic response. The mass scaling ratio was therefore set to 9.7749 × 107, to preserve solution accuracy while significantly reducing computational cost [28].

During the analysis, the ratio of kinetic to internal energy was consistently lower than 10% and ultimately reached a value of about 0.2%.

The thermal diffusion equation was solved using an implicit time integration scheme to avoid the stringent stability restrictions associated with explicit thermal solvers. The implicit formulation allows for significantly larger time steps compared to mechanical analysis. A thermal time step of $\Delta t_{mech} = 5\times 10^{-2}$s was implemented, representing a 100× increase over the mechanical time step. This staggered solution strategy preserved accuracy while significantly reducing computational cost, since temperature fields usually evolve on slower time scales than mechanical deformations.

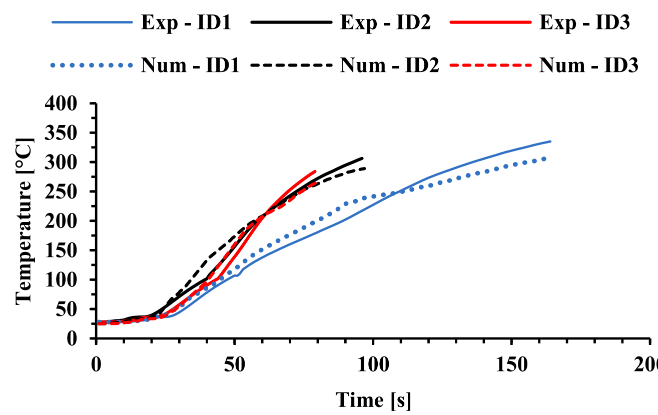

Fig. 4. Experimental vs Numerical temperature evolution for the three considered sets of input parameters.

The SPH numerical model involved four components (Fig. 3): tool, die, backing plate, and aluminum cylindrical billet (plus an aluminum sheet for flow analysis). Tools were modeled as kinematically rigid, yet AISI H13 elastic and thermal properties were assigned to ensure contact stiffness stability (please refer to paragraph 2.2.3) and accurate heat transfer, respectively [36]. The two cylindical billets were made of AA2024-T351 [37] and AA6082-T6 [38] aluminum alloys, while the thin interlayer sheet was modeled using AA5754 [39]. For these aluminum alloys, temperature-dependent thermal conductivity and heat capacity were considered. The detailed elastic and thermal properties [40,41], are shown in Table 2 while the Johnson-Cook model parameters, derived from literature, are listed in Table 3.

The computational domain was discretized using a combination of finite elements and SPH particles. The solid parts were meshed with three-dimensional four-node tetrahedral elements, characterized by an average element size of 1.7 × 10^{-3} m and a total number of 380,716 elements. Reduced integration was adopted to optimize computational efficiency while maintaining adequate accuracy in the stress and temperature fields.

For the SPH formulation, uniformly spaced particles with a diameter of 0.4 × 10^{-3} m were generated, ensuring consistent spatial resolution in all three directions. The total number of SPH particles employed in the billet domain was 263,088.

To properly model heat transfer across the interface between the SPH-discretized billet and the rigid die components, specific hybrid regions were introduced. These hybrid regions utilize rigid tetrahedral elements embedding SPH particles to establish a continuous thermal medium. Within the six-component assembly, the outer tool, inner backing plate, and inner die specifically adopt this formulation to accurately model heat conduction and thermal inertia, ensuring appropriate thermal conduction across the interface between the SPH and rigid domains. The complete simulation setup is illustrated in Fig. 3.

Time-dependent tool displacement data were acquired from the ESAB machine and used as input for the simulation. Model validation was conducted by comparing the temperatures recorded by the thermocouple embedded in the die, as well as by evaluating the agreement between the selected force and the corresponding simulated values.

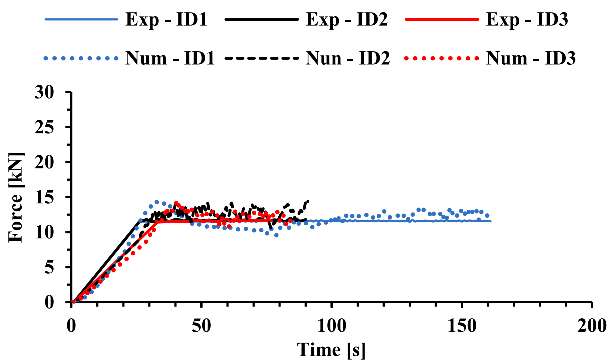

Fig. 5. Experimental vs Numerical tools' force evolution for the three considered sets of input parameters.

3. Results and discussion

3.1. Validation of the numerical model

The numerical model, developed within the SPH framework, was validated using experimental temperature and load data recorded by the thermocouple and the ESAB machine, respectively. The validation was carried out for all the process parameter combinations listed in Table to ensure the reliability and robustness of the developed numerical approach.

The results of the tuning procedure, illustrated in Fig. 4 and Fig. 5, show a satisfactory agreement between experimental and numerical results for both temperature and force. For the temperature field, a consistent match was obtained across all three parameter sets, confirming the model's capability to accurately capture the thermal evolution during the process.

Similarly, a good correlation was observed between the experimental forming forces and those predicted numerically.

An increase in the amplitude of the force oscillations, reaching approximately ±1.5 kN around the average value, was observed in correspondence with higher tool rotational speeds and consequently shorter process durations. This behavior is linked to the increase in the tool's downward velocity, which amplifies the dynamic interactions between the tool and the billet. Furthermore, the higher deformation rate associated with faster tool motion results in a more abrupt softening-hardening transition in the material response, thereby enhancing the magnitude of the force fluctuations.

3.2. Material flow investigation

In order to analyse the material flow, both cross-sectional and longitudinal sections were examined. In particular, three observations were made on the tube cross-section, on the top surface, after 5, 7, and 10 s of processing, while one study was performed on the longitudinal section of the fully extruded tubes. All the investigations refer to sample ID4. The results are presented in Fig. 6 and Fig. 7, where experimental macro images are compared with the corresponding numerical ones.

In particular, Fig. 6 shows that, as processing time increases, the material in direct contact with the tool undergoes intense mixing. For the sake of comparison, the experimentally observed material boundaries were drawn onto the numerical results, allowing a qualitative assessment of the simulation accuracy. With the experimental and numerical comparison, it is clear that after 5 s (Fig. 6a), friction mainly affects the central region of the tube cross-section, whereas after twice that time (Fig. 6c), the material mixing has already become more pronounced and extended over a wider area. It is worth noting that, although the peculiar shapes shown in Fig. 6 depend on the mechanical properties of the two considered alloys, i.e., AA2024 and AA6082, due to the moderate difference between the flow stress of the two materials, it can be accepted that similar material mixing conditions occur when the process is carried out using a solid billet or even from chips.

A clearer understanding of this phenomenon is provided by Fig. 7, which presents a comparison between the experimental and numerical longitudinal sections. It is noted that in Fig. 7b (numerical simulation)

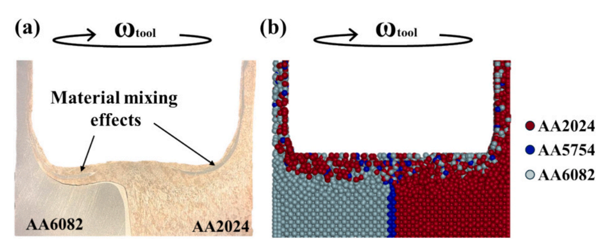

Fig. 7. Longitudinal sectional view of (a) experimental sample, (b) partial numerical simulation (only AA2024 and AA5754).

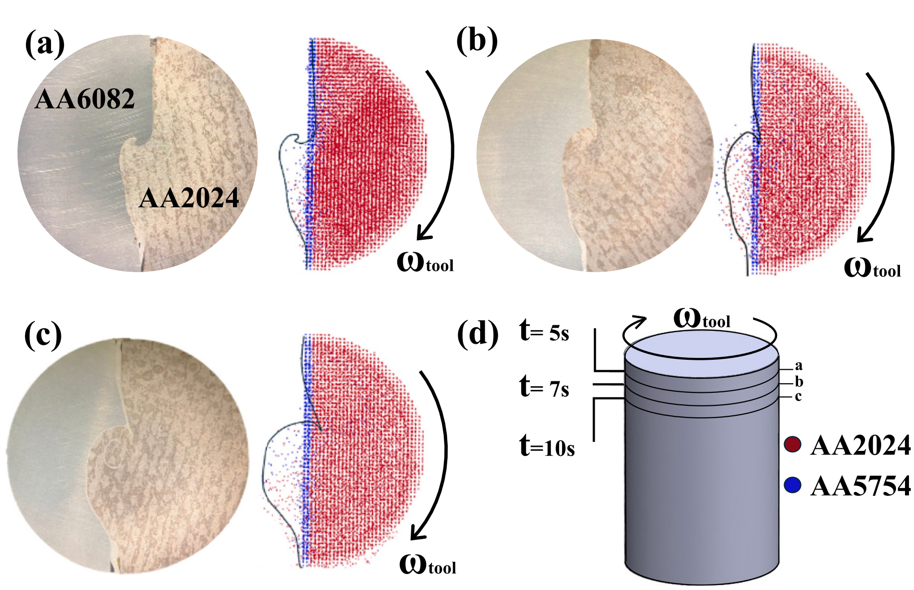

Fig. 6. Etched cross-section and numerical results of ID4 samples at three different process times: (a) 5 s, (b) 7 s, and (c) 10 s. (d) Sketch of the material layer in correspondence to the different process times.

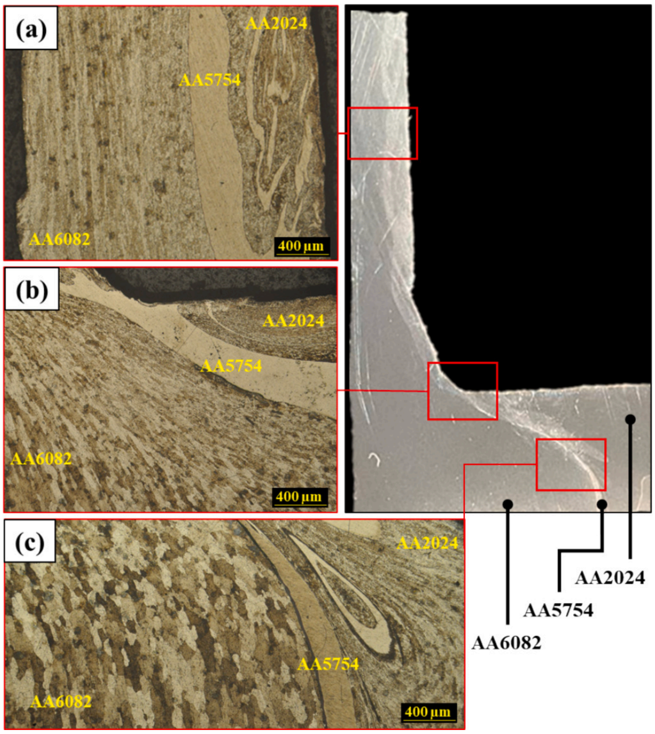

Fig. 8. Material flow images for ID4 (5× lent), at the longitudinal section of the tube.

only AA5754 and AA2024 are displayed for ease of visualization. The experimental results show that the material on the right (AA2024) experienced high stirring, forcing it to spread along the circumferential direction and eventually being extruded into the inner part of the tube thickness. On the contrary, in the outer part of the left tube wall, AA6082 is found. This material, as is already located on the left side of the original billet, undergoes lower mixing and hence strain, as better highlighted in the following.

In Fig. 8, a close-up of the edge of the tool, i.e., the zone where the actual extrusion initiates, is shown along with micro images of selected areas highlighting the grain distribution and elongation. In particular, the grains of the material not directly affected by the tool stirring, i.e., the ones in the area closer to the tube outer diameter, appear larger than those near the tool surface. This is a direct consequence of the stirring action of the tool. Moreover, this distinction remains evident across the tube thickness: finer grains are located along the inner surface, while coarser, elongated grains are confined to the outer one. Further study on grain size is provided in paragraph 3.3.

The material behavior described above can be explained by tracking the particles located within the first layer of the interlayer sheet, which acted as a marker between the two aluminum alloys. The numerical tracking clearly highlights the evolution of the sheet deformation during the process, as shown in Fig. 9. In the early stages, the particles undergo intense stirring and mixing within the region directly affected by the tool rotation, confirming the strong local shearing observed experimentally. Shortly after, the material experiences a rapid transition toward the extrusion phase, where the particle trajectories align along the extrusion direction, indicating the establishment of a steady and continuous flow.

This behavior confirms that the most significant material mixing occurs primarily at the beginning of the process, when frictional and thermal effects are at their maximum intensity, while in the following stages, the flow becomes progressively more uniform as the extrusion regime is reached. Such evidence further validates the predictive capability of the model in reproducing both the initiation of the stirring phase and the subsequent stable extrusion flow observed experimentally.

3.3. Microstructure and microhardness prediction

In order to study the effect of the tool rotation on the extruded tubes, single-material simulations were carried out. Temperature, strain, and strain rate distribution, as predicted by the numerical model, are depicted in Fig. 10 for the three considered case studies. The selected images were taken at the same process time to emphasize the effect of different rotational speeds. Looking at the temperature, it is visible that high rotational speed led to a wider heat-affected zone and faster extrusion rate (lower tool-workpiece contact interface for a given process time), which resulted in smaller strain values. With increasing tool rotation speed, two competing effects arise: the material softens and becomes easier to deform, but the shorter process time restricts the material movement following the tool and reaching large strain values. The results indicate that the latter effect predominates over the former, leading to higher strain in tubes processed at lower rotation speeds.

Additionally, as shown in Fig. 8, the experimental observations clearly revealed intense plastic deformation and significant material mixing in the region directly affected by tool rotation, corresponding to the high-strain areas identified in the simulation (Fig. 9). Conversely, the material zones in contact with the die but not directly with the tool exhibit elongated and only moderately deformed grains, similar to those that can be observed in conventional extrusion processes. This trend is well reflected in the numerical strain distribution (Fig. 10), which shows a marked decrease in strain in the outer regions of the extruded tube, where the strain values are about one order of magnitude lower than those in the inner regions.

When comparing the process variables in Fig. 10 with grain and hardness prediction (Fig. 11), the key role of temperature and strain rate appears evident. In Fig. 10, the portion of material under the tool represents the one experiencing the highest values of temperature, exhibiting values well above 300 °C, typically associated with the

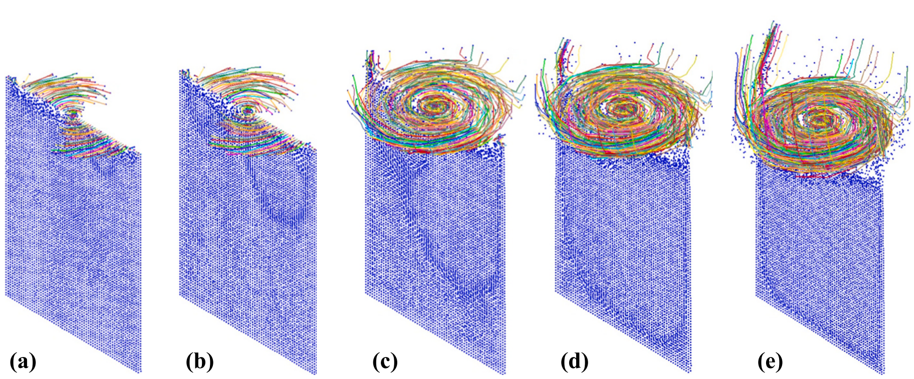

Fig. 9. Tracking of particle trajectories during the initial transient phase of extrusion at: (a) 5 s, (b) 10 s, (c) 20 s, (d) 30 s, and (e) 40 s.

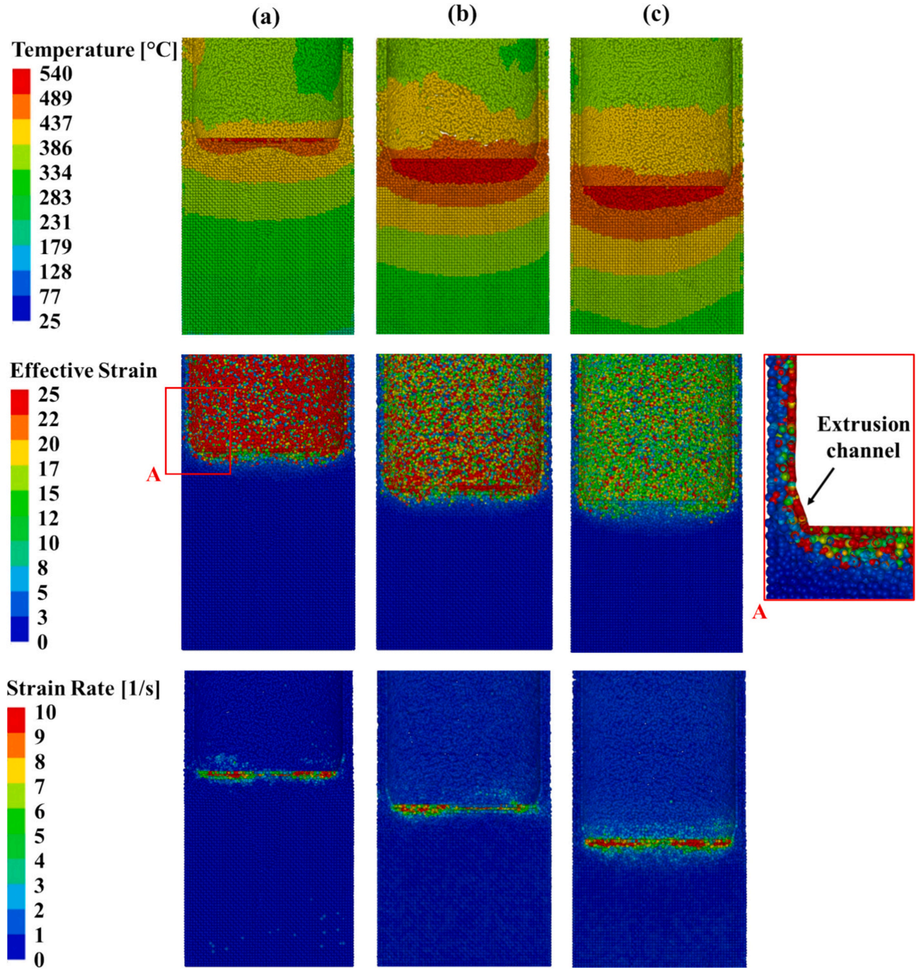

Fig. 10. Temperature, effective strain, and strain rate distributions for (a) ID1, (b) ID2, and (c) ID3. A close-up of the corner area is presented in "A".

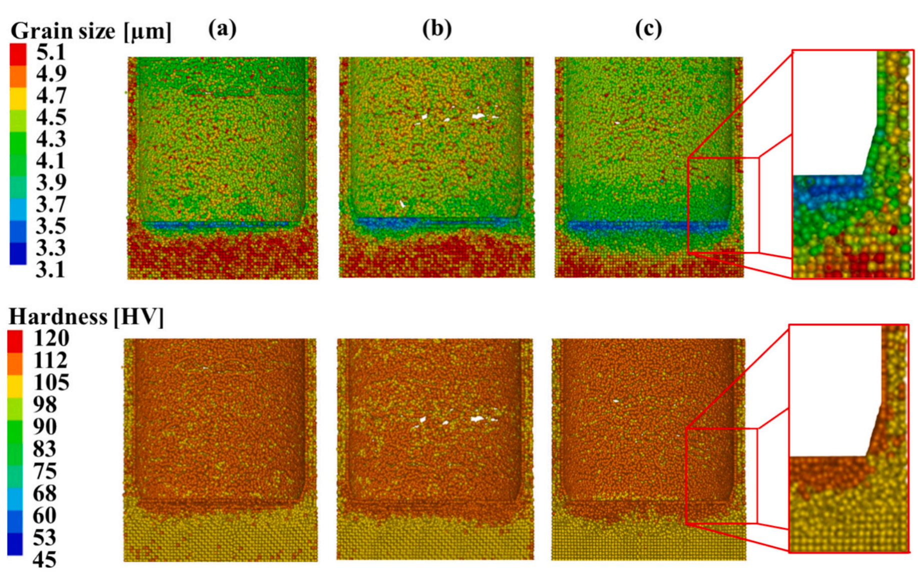

Fig. 11. Grain size and hardness distribution for (a) ID1, (b) ID2, and (c) ID3.

recrystallization temperature threshold of most aluminum alloys.

The combination of elevated temperature and high strain levels promoted visible grain refining (Fig. 11c). During the process, this refined material is stirred and extruded, remaining distinct from the outer layers that are less influenced by the tool (see region "A" in Fig. 8), as highlighted in the previous paragraph through the particle tracking. Analyzing the average grain size distribution across the tube, it is observed that directly under the tool, the grain size ranges between 3.3

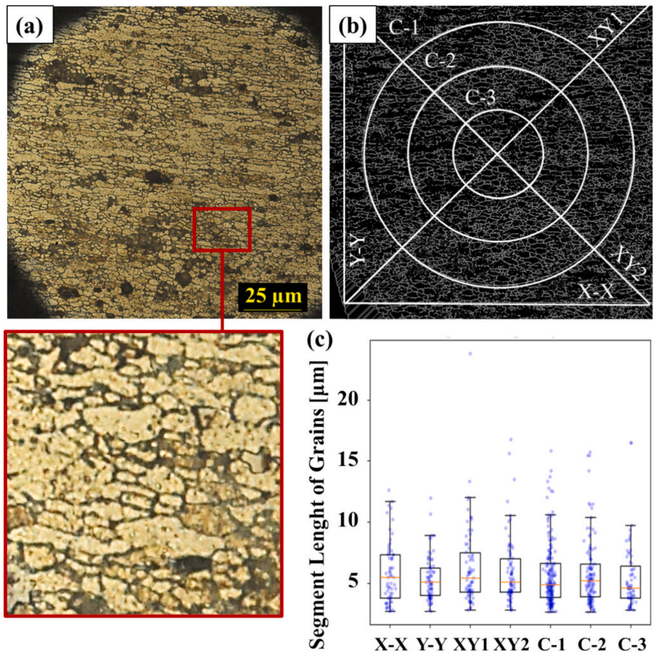

Fig. 12. Automated grain size analysis according to ASTM E112–13: (a) specimen micrograph, (b) grain boundary skeletonization, and (c) automatic grain diameter detection along seven measurement paths.

and 3.7 μm. Moving toward the extrusion channel, the reduced strain and the elevated temperature promote grain coarsening, with the size increasing up to approximately 4.3 μm. Along the tube thickness, this effect of intense strain due to the extrusion is clearly evident: a finer grain layer is found near the inner surface (around 3.7 μm), whereas the grain size gradually increases toward the outer surface, reaching about 4.7 μm (as already discussed previously.

These behaviours are further corroborated by the experimental results obtained through automated grain measurements reported in Fig. 12, which visually illustrates the automatic acquisition process for the specimen ID3 (middle surface of the tube's wall). In this transition area between the inner and outer tube surface, both moderately elongated grains and equiaxed ones are observed, with an average dimension of 4.8 μm, indicating that recrystallization phenomena occurred before the further deformation due to the actual extrusion mechanics.

The results of this measurement procedure are reported in Fig. 13, which compares the experimental data obtained at different rotational speeds. The longitudinal section shows that the largest grains are located under the tool and near the extrusion channel (points A and B in Fig. 13), with average sizes of 4.5 μm and 4.0 μm, respectively. The only exception is case ID3, where the elevated temperatures lead to grain coarsening; as it is shown in Fig. 10, ID3 experiences the highest thermal exposure, particularly in the region directly under the tool. Moving toward the tube wall (points C and D in Fig. 13), the grain size decreases with an overall average of 3.8 μm. These findings are consistent with the grain distribution predicted numerically (Fig. 11), with a calculated average error of 8.5%.

Moreover, a clear correlation emerges between grain size and hardness. The highest hardness values, around 108 HV, occur in regions characterized by finer grains, whereas approximately 98 HV is measured under the tool where coarser grains are present.

In addition, Fig. 14 compares the experimental and numerical microhardness distributions for the ID3 cross-section. Lower values (94–98 HV) are observed beneath the tool, while higher values (∼102–108 HV) appear across the tube thickness. This agreement is validated by a quantitative assessment showing an average error of 5.4%. Specifically, local deviations are 4.1% in the bulk, 6.7% at the corner radius, and 5.5% along the side wall. These discrepancies confirm the SPH model's accuracy in predicting the through-thickness gradient and the micro-mechanical response of the tube.

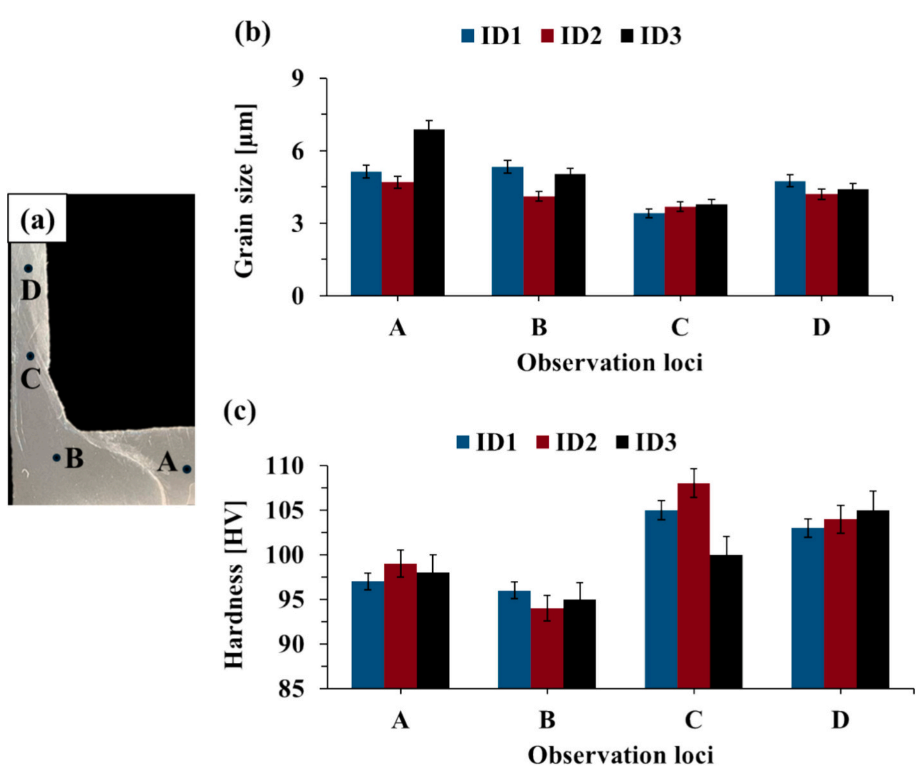

Fig. 13. (a) Experimental observation loci for (b) grain and (c) hardness measurement, at different rotational speeds.

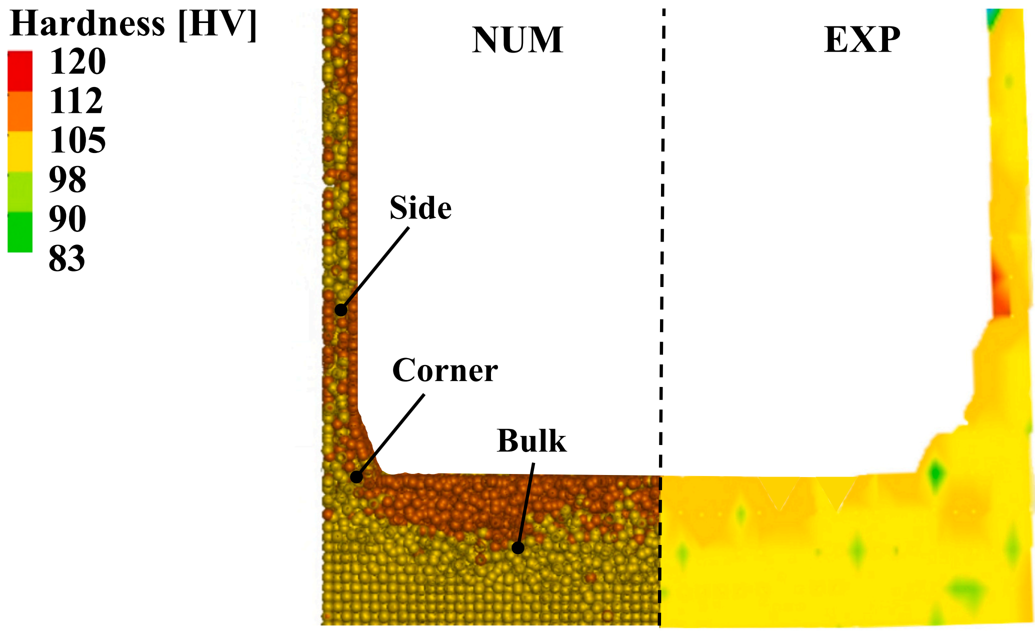

Fig. 14. Numerical and experimental hardness comparison for ID3.

4. Summary and Conclusions

In this paper, a dedicated numerical model based on the SPH technique was developed, validated, and used to simulate the friction stir extrusion of tubes from solid billets of different aluminum alloys. Experimental tests were developed to validate the model with respect to temperatures and loads on the tool. The numerical model was then utilized to get insights into the process mechanics, through the prediction of the material flow during the process, as well as to predict the microstructure and microhardness of FSEed tubes. Based on the results obtained, the following conclusion can be drawn:

- Both experimental and numerical analyses revealed that intense stirring phenomena occur on layers adjacent to the tool bottom surface, leading to recrystallization. The fine-grain material is displaced toward the inner tube surface, forming a distinct layer separated from the elongated and less deformed grain zone close to the tube external diameter.
- Numerical simulations revealed that the region under the tool undergoes the highest temperatures, with values increasing with increasing tool rotational speed. This condition promotes elevated strain rate and strain level. However, as the rotational speed increases, the strain decreases due to the concurring increase in the extrusion rate, resulting in lower processing times for a given material zone.
- Microstructure and microhardness analyses indicated that the mechanical stirring generated by the tool led to grain refining (avg. 3.8 μm) along tube walls, and a corresponding hardness value of avg. 105 HV. The overall grain hardness resulted in agreement with the Hall-Petch relationship.
- The developed SPH-based prediction tool exhibited high accuracy and effectiveness in reproducing the evolution of both grain size and hardness throughout the extruded tube, confirming its capability as a predictive and design-support instrument for FSE processes.

Future work includes the use of the developed tool to properly design the process, both in terms of tool geometry and main process parameters, in order to obtain as homogeneous as possible microstructural and mechanical properties across the tube wall thickness.

CRediT authorship contribution statement

Salvatore Russo: Formal analysis, Writing – original draft. **Riccardo Puleo:** Formal analysis, Writing – original draft. **Gianluca Buffa:** Methodology, Supervision, Writing – original draft, Writing – review & editing. **Livan Fratini:** Supervision, Writing – review & editing.

Declaration of competing interest

The Authors disclose no actual or potential conflict of interest that could inappropriately influence, or be perceived to influence, this work.

Acknowledgements

This study was carried out within the MICS (Made in Italy – Circular and Sustainable) Extended Partnership and received funding from the European Union Next-Generation EU (PIANO NAZIONALE DI RIPRESA E RESILIENZA (PNRR) – MISSIONE 4 COMPONENTE 2, INVESTIMENTO 1.3 – D.D. 1551.11–10-2022, PE00000004). This manuscript reflects only the authors' views and opinions, neither the European Union nor the European Commission can be considered responsible for them.

References

[1] Duflou JR, Wegener K, Tekkaya AE, Hauschild M, Bleicher F, Yan J, et al. Efficiently preserving material resources in manufacturing: industrial symbiosis revisited. CIRP Ann 2024;73:695–721. https://doi.org/10.1016/j.cirp.2024.05.006.
[2] Raabe D, Ponge D, Uggowitzer PJ, Roscher M, Paolantonio M, Liu C, et al. Making sustainable aluminum by recycling scrap: The science of “dirty” alloys. Prog Mater Sci 2022;128. https://doi.org/10.1016/j.pmatsci.2022.100947.
[3] Baffari D, Reynolds AP, Li X, Fratini L. Influence of processing parameters and initial temper on Friction Stir Extrusion of 2050 aluminum alloy. J Manuf Process 2017;28:319–25. https://doi.org/10.1016/j.jmapro.2017.06.013.
[4] Behnagh RA, Shen N, Ansari MA, Narvan M, Kazem M, Givi B, et al. Experimental analysis and microstructure modeling of friction stir extrusion of magnesium chips. J Manuf Sci E T ASME 2016;138. https://doi.org/10.1115/1.4031281.
[5] Whalen S, Olszta M, Roach C, Darsell J, Graff D, Reza-E-Rabby M, et al. High ductility aluminum alloy made from powder by friction extrusion. Materialia (Oxf) 2019;6. doi:https://doi.org/10.1016/j.mtla.2019.100260.
[6] Li L, Gupta V, Li X, Reynolds AP, Grant G, Soulami A. Meshfree simulation and experimental validation of extreme thermomechanical conditions in friction stir extrusion. Comput Part Mech 2022;9:789–809. https://doi.org/10.1007/s40571-021-00445-7.

[7] Behnagh RA, Fathi F, Yeganeh M, Paydar M, Mohammad MA, Liao Y. Production of seamless tube from aluminum machining chips via double-step friction stir consolidation. Int J Adv Manuf Technol 2019;104:4769–77. https://doi.org/10.1007/s00170-019-04326-5.
[8] Swarnkar R, Karmakar S, Pal SK. An investigation of bimetallic tube fabrication through a novel friction stir extrusion based technology for automotive applications. Mater Today Commun 2023;35. https://doi.org/10.1016/j.mtcomm.2023.106363.
[9] Asadi P, Akbari M, Sadowski T, Asl YD, Choupani N, Bedir F. Examining the impact of tool taper angle in Al-Si tube manufacturing by friction stir extrusion. J Manuf Process 2024;131:532–44. https://doi.org/10.1016/j.jmapro.2024.09.047.
[10] Lucy LB. A numerical approach to the testing of the fission hypotesis. Astron J 1977;82:1013–24.
[11] Gingold RA, Monaghan JJ. Smoothed particle hydrodynamics: theory and application to non-spherical stars. Mon Not R Astron Soc 1977;181:375–89.
[12] Monaghan JJ. Smoothed particle hydrodynamics. Rep Prog Phys 2005;68:1703–59. https://doi.org/10.1088/0034-4885/68/8/R01.
[13] Liu MB, Liu GR. Smoothed particle hydrodynamics (SPH): An overview and recent developments. Archives of Computational Methods in Engineering 2010;17:25–76. https://doi.org/10.1007/s11831-010-9040-7.
[14] He QG, Chen X, Chen JF. Finite element-smoothed particle hydrodynamics adaptive method in simulating debris cloud. Acta Astronaut 2020;175:99–117. https://doi.org/10.1016/j.actaastro.2020.05.056.
[15] Ba K, Gakwaya A. Thermomechanical total Lagrangian SPH formulation for solid mechanics in large deformation problems. Comput Methods Appl Mech Eng 2018;342:458–73. https://doi.org/10.1016/j.cma.2018.07.038.
[16] Fraser K, Kiss LI, St-George L. Adaptive Thermal Boundary Conditions for Smoothed Particle Hydrodynamics. n.d.
[17] Zhang Z, Shu C, Khalid MSU, Liu Y, Yuan Z, Jiang Q, et al. SPH modeling and investigation of cold spray additive manufacturing with multi-layer multi-track powders. J Manuf Process 2022;84:565–86. https://doi.org/10.1016/j.jmapro.2022.10.032.
[18] Komen H, Shigeta M, Tanaka M. Numerical simulation of molten metal droplet transfer and weld pool convection during gas metal arc welding using incompressible smoothed particle hydrodynamics method. Int J Heat Mass Transf 2018;121:978–85. https://doi.org/10.1016/j.ijheatmasstransfer.2018.01.059.
[19] Nassiri A, Zhang S, Lee T, Abke T, Vivek A, Kinsey B, et al. Numerical investigation of CP-Ti & Cu110 impact welding using smoothed particle hydrodynamics and arbitrary Lagrangian-Eulerian methods. J Manuf Process 2017;28:558–64. https://doi.org/10.1016/j.jmapro.2017.04.032.
[20] Zhang ZL, Liu MB. Numerical studies on explosive welding with ANFO by using a density adaptive SPH method. J Manuf Process 2019;41:208–20. https://doi.org/10.1016/j.jmapro.2019.03.039.
[21] YANG M, ZHANG B yuan, MA H hao, WANG J xiang, XIONG J yi. Microstructure and grain evolution mechanisms of copper/steel explosive welding interface. Transactions of Nonferrous Metals Society of China (English Edition) 2024;34:1588–605. doi:https://doi.org/10.1016/S1003-6326(24)66493-9, Trans Nonferrous Metals Soc China.
[22] Li L, Garcia D, Wang T, Escobar JD, Pole M, Nwe K, et al. Meshfree simulation and prediction of recrystallized grain size in friction stir processed 316L stainless steel. J Mater Process Technol 2025;337. doi:https://doi.org/10.1016/j.jmatprotec.2025.118751.
[23] Li L, Reza-E-Rabby M, Overman N, Wang T, Whalen S, Grant G, et al. Analysis of contact conditions and microstructure evolution in shear assisted processing and extrusion using smoothed particle hydrodynamics method. Mater Des 2022;221. doi:https://doi.org/10.1016/j.matdes.2022.111010.
[24] Baffari D, Buffa G, Fratini L. A numerical model for Wire integrity prediction in Friction Stir Extrusion of magnesium alloys. J Mater Process Technol 2017;247:1–10. https://doi.org/10.1016/j.jmatprotec.2017.04.007.
[25] Puleo R, Latif A, Ingarao G, Di Lorenzo R, Fratini L. Solid bonding criteria design for aluminum chips recycling through friction stir consolidation. J Mater Process Technol 2023;319. https://doi.org/10.1016/j.jmatprotec.2023.118080.
[26] Li X, Cui L, Li J, Chen Y, Han W, Shonkwiler S, et al. Automation of intercept method for grain size measurement: a topological skeleton approach. Mater Des 2022;224. doi:https://doi.org/10.1016/j.matdes.2022.111358.
[27] Elbossily A, Kallien Z, Chafle R, Fraser KA, Afrasiabi M, Bambach M, et al. GPU-accelerated meshfree computational framework for modeling the friction surfacing process. Comput Part Mech 2025. https://doi.org/10.1007/s40571-025-01048-2.
[28] Li L, Gupta V, Li X, Reynolds AP, Grant G, Soulami A. Meshfree simulation and experimental validation of extreme thermomechanical conditions in friction stir extrusion. Comput Part Mech 2022;9:789–809. https://doi.org/10.1007/s40571-021-00445-7.
[29] Taylor GI, Society R, Qu In N E Y H. The Latent Energy Remaining in a Metal after Cold Working. n.d.
[30] Hu F, Chen G, Lin Y, Wang H, Zhu Z. Numerical and experimental study on the thermal process during additive friction stir deposition. CIRP J Manuf Sci Technol 2024;48:55–66. https://doi.org/10.1016/j.cirpj.2023.12.002.
[31] Duan X, Sheppard T. Influence of forming parameters on the final subgrain size during hot rolling of aluminium alloys. n.d.
[32] Zaidi MA, Sheppard T. Development of microstructure throughout roll gap during rolling of aluminium alloys. 1982.
[33] Genevois C, Deschamps A, Denquin A, Doisneau-Cottignies B. Quantitative investigation of precipitation and mechanical behaviour for AA2024 friction stir welds. Acta Mater 2005;53:2447–58. https://doi.org/10.1016/j.actamat.2005.02.007.
[34] Sonne MR, Tutum CC, Hattel JH, Simar A, De Meester B. The effect of hardening laws and thermal softening on modeling residual stresses in FSW of aluminum alloy 2024-T3. J Mater Process Technol 2013;213:477–86. https://doi.org/10.1016/j.jmatprotec.2012.11.001.
[35] Sato YS, Urata M, Kokawa H, Ikeda K. Hall-Petch relationship in friction stir welds of equal channel angular-pressed aluminium alloys. Mater Sci Eng A 2003;354:298–305. https://doi.org/10.1016/S0921-5093(03)00008-X.
[36] Afazov SM, Ratchev SM, Segal J. Prediction and experimental validation of micro-milling cutting forces of AISI H13 steel at hardness between 35 and 60 HRC. Int J Adv Manuf Technol 2012;62:887–99. https://doi.org/10.1007/s00170-011-3864-7.
[37] Johnson GR, Cook WH. A constitutive model and data for metals subjected to large strains, high strain rates and high temperatures. Proceedings of the 7th International Symposium on Ballistics. The Hague, Netherlands. 1983.
[38] Fang N. A new quantitative sensitivity analysis of the flow stress of 18 engineering materials in machining. J Eng Mater Technol 2005;127:192–6. https://doi.org/10.1115/1.1857935.
[39] Liu Y, Ge M, Zeng G, Wang Z, Chen K, Yin X, et al. Process analysis and multi-parameter optimization of 5052 aluminum alloy FSW based on thermo-mechanical coupling and Taguchi method. Sci Rep 2025;15. doi:https://doi.org/10.1038/s41598-024-82923-5.
[40] ASM International. Handbook Committee. Properties and Selection–Irons, Steels, and High-performance Alloys2. ASM international; 1990.
[41] Afazov SM, Ratchev SM, Segal J. Prediction and experimental validation of micro-milling cutting forces of AISI H13 steel at hardness between 35 and 60 HRC. Int J Adv Manuf Technol 2012;62:887–99. https://doi.org/10.1007/s00170-011-3864-7.